Opto-Electronic Advances

CN 51-1781/TN ISSN (Print) 2096-4579 ISSN (Online) 2097-3993

Luminescent YAG:Ce^{3+} 3D micro-structures via multi-photon laser lithography

Robertas Virkėtis, Greta Merkininkaitė*, Artūr Harnik, Ugnė Ūsaitė, Dominykas Dapšys, Arturo Susarrey-Arce, Simas Šakirzanovas and Mangirdas Malinauskas*

Citation: Virkėtis R, Merkininkaitė G, Harnik A et al. Luminescent YAG:Ce^{3+} 3D micro-structures via multi-photon laser lithography. *Opto-Electron Adv* **9**, 250338 (2026).

https://doi.org/10.29026/oea.2026.250338

Received: 1 December 2025; Accepted: 27 April 2026; Published online: 4 June 2026

OEA | Opto-Electronic Advances

Article

August 2026, Vol. 9, No. 8

Open Access

Luminescent YAG:Ce^{3+} 3D micro-structures via multi-photon laser lithography

Robertas Virkėtis[1], Greta Merkininkaitė[1]*, Artūr Harnik[3], Ugnė Ūsaitė[1], Dominykas Dapšys[3], Arturo Susarrey-Arce[4], Simas Šakirzanovas[1,2] and Mangirdas Malinauskas[3]*

Abstract: This work addresses the challenge of fabricating crystalline single-phase luminescent 3D microstructures by demonstrating a fabrication process of yttrium aluminum garnet doped with cerium (YAG:Ce^{3+}) 3D micro-objects. Precursors were synthesized via a sol-gel method and characterized by refractive index (RI) measurements, Fourier-transform infrared spectroscopy (FT-IR), and thermogravimetric (TG) analysis to verify chemical composition changes during photopolymerization and thermal treatment. Multiphoton laser 3D lithography (MP3DL) was employed to produce hybrid metal-organic 3D structures, which were subsequently converted into crystalline ceramics through controlled 3-step annealing. Structural analysis by X-ray diffraction (XRD) confirmed the formation of single-phase cubic YAG across Ce^{3+} concentrations up to 5 mol-% in 3D objects, while scanning electron microscopy (SEM) revealed isotropic shrinkage (ca. 39%) and well-preserved geometries with sub-micrometer features after pyrolysis. The smallest feature of a crystalline 3D object achieved was 0.48 µm with a spatial resolution down to 2.4 µm. Luminescence measurements showed characteristic Ce^{3+} emission centered at 558 nm, with maximum intensity at 2 mol-% doping. These findings establish a reliable pathway to fabricate thermally stable, high-resolution, luminescent single-phase YAG:Ce^{3+} 3D micro-objects, enabling their integration into optoelectronic and photonic applications.

Keywords: non-linear optics; laser lithography; multiphoton 3D polymerization; nanostructuring; active materials; luminescence; integrated photonics; ceramics; durability; material engineering

DOI: 10.29026/oea.2026.250338 | CSTR: 32247.14.oea.2026.250338

Citation: Virkėtis R, Merkininkaitė G, Harnik A et al. Luminescent YAG:Ce^{3+} 3D micro-structures via multi-photon laser lithography. *Opto-Electron Adv* **9**, 250338 (2026).

1 Introduction

Ceramics —crystalline inorganic materials such as oxides, nitrides, fluorides, and sulfides —play a pivotal role in modern photonics, underpinning technologies ranging from optical fibers and switches to laser amplifiers and radiation detectors[1–3]. Their exceptional mechanical strength, high thermal[4] and chemical stability, and resilience under extreme environmental conditions make them indispensable for applications even in space environments. Depending on the processing route, ceramics can be obtained as thin films, fibers, or fully three-dimensional (3D) architectures, exhibiting optical transmittance from the deep ultraviolet (UV) to the near-infrared (NIR) range. Importantly, perfect transparency is not always required: in luminescent materials, moderate light scattering can enhance color mixing and diffusion, enabling high-brightness lighting, projectors, and sensing systems[5–9].

Optical and functional performance in ceramics strongly depends on their phase purity and microstructure[10]. Single-phase crystalline ceramics, even when polycrystalline, exhibit a chemically and structurally homogeneous composition, ensuring uniform optical and electronic properties. The absence of a secondary phase in the ceramic eliminates extraneous emission centers and non-radiative pathways, thereby enhancing luminescence intensity and stability[11]. In

Received: 1 December 2025

Accepted: 27 April 2026

Published online: 4 June 2026

[1]Faculty of Chemistry and Geosciences, Vilnius University, Naugarduko Str. 24, Vilnius LT-03225, Lithuania; [2]Department of Chemical Engineering and Technology, Center for Physical Sciences and Technology, Saulėtekio Ave. 3, Vilnius LT-10257, Lithuania; [3]Laser Research Center, Physics Faculty, Vilnius University, Saulėtekio Ave. 10, Vilnius LT-10223, Lithuania; [4]Department of Chemical Engineering, Mesoscale Chemical Systems, MESA+ Institute, University of Twente, P.O. Box 217, Enschede 7500 AE, Netherlands.

*Correspondence: G Merkininkaitė, E-mail: greta.merkininkaite@chgf.vu.lt; M Malinauskas, E-mail: mangirdas.malinauskas@ff.vu.lt

comparison to multiphase systems, single-phase crystalline materials thus demonstrate superior light-emission efficiency, reproducibility, and predictability of functional response, which is crucial for photonic integration and device reliability.

Among oxide ceramics, yttrium aluminum garnet (YAG) stands out as a benchmark host for optically active ions. Cerium-doped YAG (YAG:Ce^{3+}) is a well-known yellow phosphor with a broad emission band centered around 560 nm, originating from the $[Xe]5d^1 \rightarrow [Xe]4f^1$ transition of Ce^{3+} under 300–500 nm excitation[12]. Owing to its highly intense yellow emission, thermal stability, and robustness, YAG:Ce^{3+} underpins diverse technologies such as solid-state lasers, white LEDs, scintillators, and integrated photonic devices[13–16].

Recent advances in additive manufacturing have enabled the 3D printing of luminescent ceramics, including YAG:Nd, YAG:Yb, and YAG:Ce[17–23]. However, these structures are typically produced at millimeter or centimeter scales and often consist of amorphous or multiphase polycrystalline domains[17,21]. Achieving microscale, compositionally pure, and crystalline luminescent architectures has remained a significant challenge due to the complex interplay between precursor chemistry, photopolymerization, and high-temperature crystallization.

The multiphoton 3D lithography (MP3DL) technique, originally developed for organic photoresists[24], is now being extended to the high-resolution additive manufacturing of inorganic materials[25], especially through hybrid sol-gel precursors[26–28]. Recent breakthroughs, including the two-photon printing of fused silica from silicon-based resins[29,30] of high-precision glass optics, reflect the substantial and rapidly intensifying research activity within this area. However, though these approaches are very encouraging as they enable lower-temperature treatment, they fundamentally remain restricted to amorphous glass. In contrast, our work targets single-phase crystalline ceramic architectures, where controlled crystallization requires higher thermal treatment, but yields phase purity, expanded functionality, and stability that are inaccessible in silica systems. This positions our approach as an advanced direction within MP3DL, extending the technique toward functional single-phase crystalline microstructures relevant to integrated photonics and optoelectronics[31], including waveguides and light-redirecting photonic crystals[32,33]. Combining and integrating YAG:Ce and other phosphor 3D microstructures into a single device could also be used to achieve directed white-light emission. Alternatively, YAG:Dy can be used directly to achieve this[34].

In this work, we demonstrate for the first time the fabrication of single-phase crystalline luminescent 3D microstructures. This is much different from other works where YAG:Ce, YAG:Ce in glass or other phosphors were studied as powders or ceramic films[35–44] as here the emphasis is put on fabrication of monophasic YAG:Ce microstructures. By combining tailored sol-gel precursor synthesis, MP3DL, and a precisely controlled multi-step heat-treatment protocol, we successfully produced single-phase polycrystalline YAG:Ce^{3+} 3D microarchitectures exhibiting strong, spatially uniform luminescence, as shown in Fig. 1. The phase purity of the

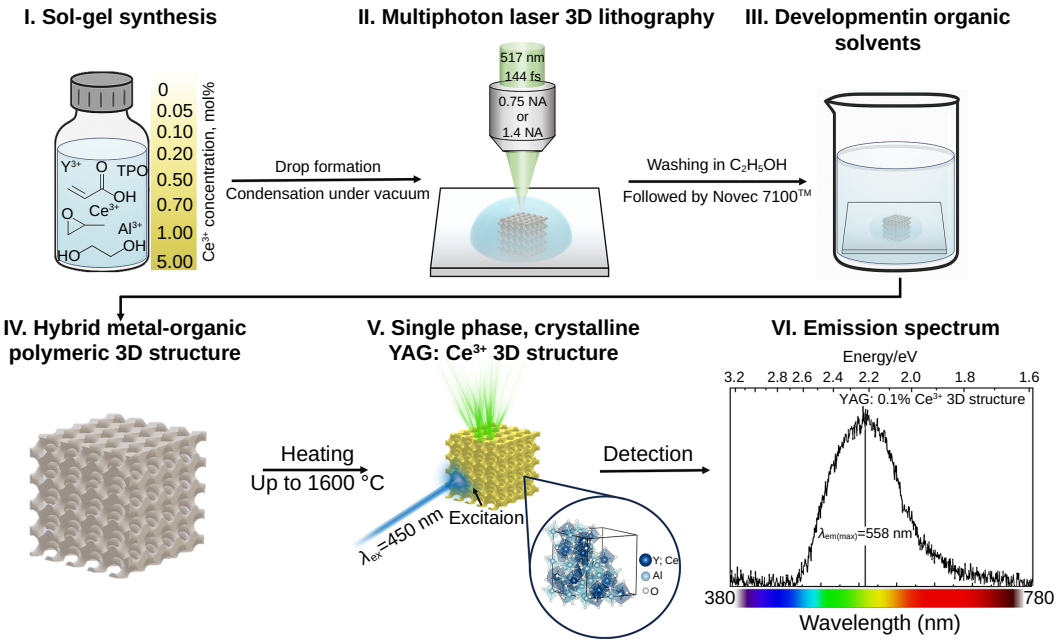

Fig. 1 | Schematic illustration of the fabrication and characterization process of YAG:Ce^{3+} 3D microstructures. A photoresin was prepared with varying Ce^{3+} concentrations (0–5 mol-%) and then it was structured via MP3DL, followed by development and pyrolysis, to yield crystalline, single-phase, luminescent YAG:Ce^{3+} 3D microstructures. The resulting microstructures exhibit a characteristic Ce^{3+} emission band peaking at 558 nm under 450 nm excitation, confirming the successful formation of the cubic YAG:Ce single-phase and its luminescent functionality.

resulting material ensures maximized emission efficiency, while the crystalline yet polycrystalline nature of the structures provides mechanical robustness and uniformity at the microscale. The smallest achieved feature size of (0.50 ± 0.03) μm highlights the high spatial precision of this method and its potential for integration into future miniaturized photonic systems.

2 Results and discussion

2.1 Evaluation of refractive indices of YAG precursors

The initial characterization of the synthesized materials involves evaluating their refractive indices (RI). In MP3DL, polymerization is triggered only at the laser focus, where two photons are absorbed simultaneously. The RI of the prepared YAG precursor sols, gels, and polymers plays a crucial role in determining their transmittance to electromagnetic waves, while simultaneously affecting the intensity distribution defining the size and shape of the produced voxel. In case of a significant mismatch with the glass optics (as well as the glass or sapphire coverslip) an additional precompensation coefficient must be established for the manufacturing, which corresponds to the specific material's RI[45]. To maintain the correct proportions of the printed 3D structure in the *Z*-direction, the design model must be prescaled along the optical axis by dividing its *Z*-dimensions by the effective refractive index of the resin. This compensates for the optical path lengthening caused by the higher refractive index of the material compared to air.

Figure 2 illustrates the RI dependence on wavelengths ranging from 436.5 to 643.3 nm for YAG:Ce^{3+} precursor mixtures at different synthesis stages, including formation of sols, gels and polymers: (a) 0%, (b) 0.5% and (c) 2%. Meanwhile, Fig. 2(d–f) show the RI dependence on wavelength for sols, gels, and polymers, respectively, across a wide range of Ce^{3+} dopant concentrations (0–5 mol-%). It is obvious that the RI of all synthesized materials decrease as the wavelength increases. As the synthesis of sol-gel materials progresses through different stages —from hydrolysis and condensation to polymerization —the RI increase, confirming the densification of YAG:Ce^{3+} precursors[46]. The consistency of dependency deviation coefficients, as the RI decrease with increasing wavelength across different synthesis stages and sample concentrations, confirms the homogeneity of the materials. Materials with a higher concentration of cerium dopant tend to have slightly lower RI (see Fig. 2(d–f)). However, the difference in RI is minimal, varying only in the second or third decimal place (for example, in sols from 1.455 to 1.454, in gels from 1.477 to 1.468, and in polymers from 1.482 to 1.468 at 436.5 nm). The highest RI across the entire wavelength range is observed in undoped YAG polymer material, with a value of 1.482 at 436.5 nm, while the lowest is in the YAG sol precursor doped with 0.7 mol-% Ce^{3+} ions, with a value of 1.439 at 643.3 nm. The standard deviation values in sols and gels are 0.005 and 0.006 in polymers. This minor difference in RI is insignificant, indicating that all synthesized YAG:Ce^{3+} precursors, with Ce^{3+} molar concentrations ranging from 0 to 5 mol-%, are suitable for polymerization within the wavelength range of 436.5 nm to 643.3 nm, using the same fabrication coefficient for all materials.

The most important conclusion from the RI measurements is that the RI of the gels ranges from 1.454 to 1.479 (see Fig. 2(e)), which matches the RI of the coverslip ($RI \approx 1.517$) and immersion oil ($RI \approx 1.516$). This makes the material highly suitable for polymerization using immersion oil objectives. Compared to non-immersion objectives, immersion lenses allow for tighter focusing, which enables the fabrication of features with smaller dimensions. In addition, the focal point can be positioned deep within the material, allowing for the fabrication of tall structures with consistent properties throughout their height.

2.2 Changes in chemical structure: from hybrid resin to inorganic YAG

Fourier transform infrared spectroscopy (FT-IR) analysis was performed to identify the chemical bonds and structural changes occurring in the synthesized materials. The FT-IR spectra were measured for YAG sols, gels, polymers, and derivatives calcined at 800 °C, doped with varying concentrations of Ce^{3+} ions (0–5 mol-%). The obtained spectra revealed that Ce^{3+} ion concentrations up to 5% did not influence the intensity or position of the peaks. For further IR analysis, undoped and 2% Ce^{3+}-doped YAG samples were selected, as the latter exhibits the most intense emission (as will be discussed in the Section 2.6 *Investigation of optical properties*).

Figure 3 shows FT-IR spectra of undoped YAG and YAG:2% Ce^{3+} sols (a), gels (b), polymers (c) and derivatives calcined at 800 °C (d). In the IR spectra of sols (a), gels (b) and polymers (c) broad and intense peaks observed near 3350 cm^{-1} correspond to the O–H bond vibrations. The decrease in the intensity of these peaks in gels (Fig. 3(b)) indicates that, as the sol condenses, solvent partial evaporation occurs. Additionally, other intense peaks are observed: 2965 cm^{-1} and 2840 cm^{-1} correspond to asymmetric and symmetric CH_2; 1425 cm^{-1} corresponds to COO^-; 1300 cm^{-1} indicates C–O; 1200 cm^{-1} relates to C–C; 1085–1034 cm^{-1} represent Me–O–C bond vibrations. In Fig. 3(b), Y, Al and Ce are observed by looking at the Me–O bond vibrations at 500 cm^{-1}. These formed bonds confirm the successful formation of metal-organic complexes, which are at least partially formed with acrylic acid (monomer), since the same peaks are also visible in the polymer (indicating a successful incorporation of metal ions into the polymer. Peaks observed at 1640 cm^{-1}, corresponding to C=C bond vibrations, show significantly reduced intensity in the polymer spectrum (Fig. 3(c)) compared to those in the sol

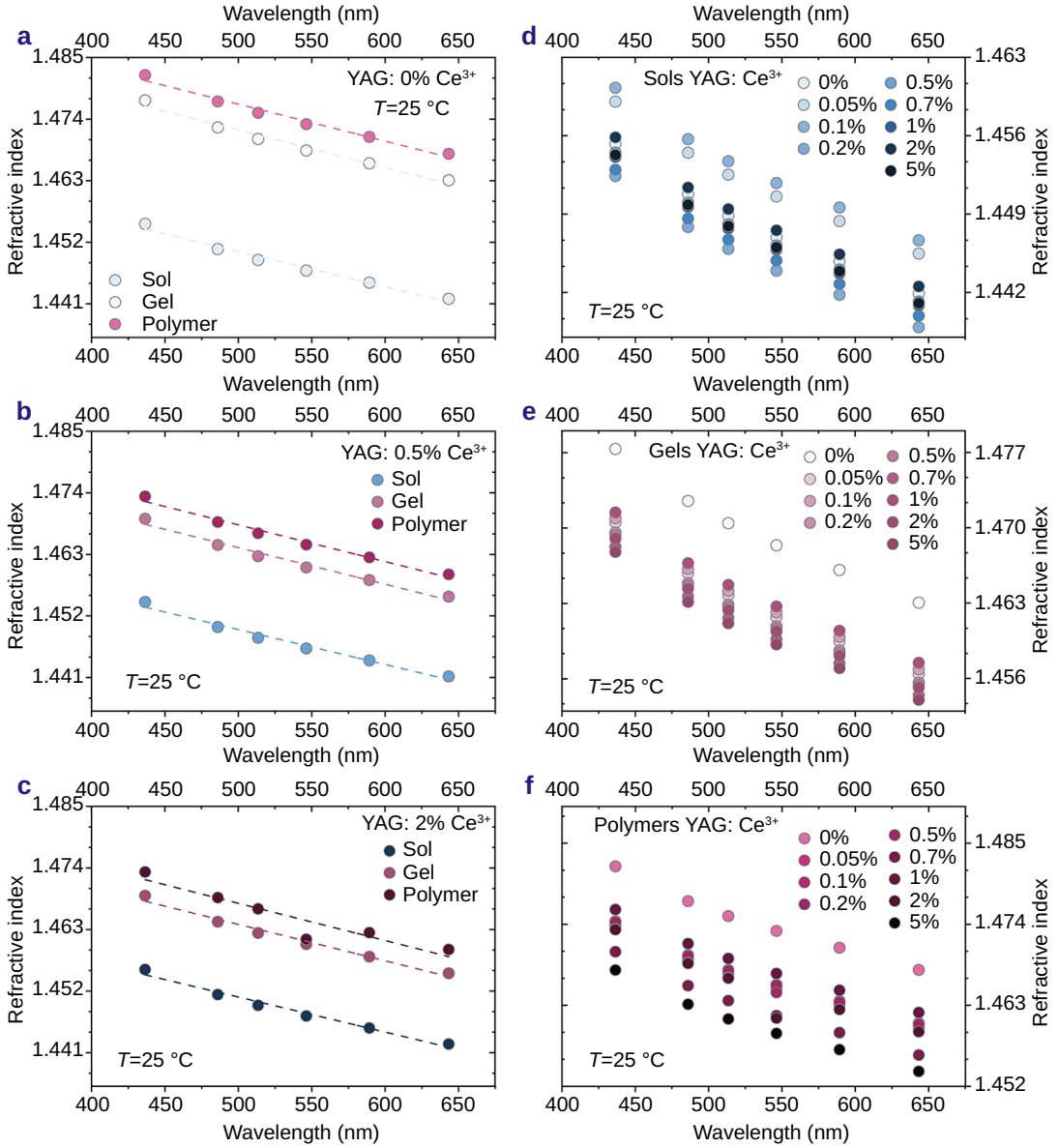

Fig. 2 | RI of (a) YAG:0% Ce^{3+}, (b) YAG:0.5% Ce^{3+}, (c) YAG:2% Ce^{3+} precursors at different synthesis stages, and refractive indices of YAG:Ce^{3+} (d) sols, (e) gels and (f) polymers at varying Ce^{3+} molar concentration (0, 0.05, 0.1, 0.2, 0.5, 0.7, 1, 2, 5 mol-%) as a function of wavelength at 25 °C. RI measurements showed that, regardless of the Ce^{3+} content in the material, the parameters of the photopolymerization system can remain unchanged, as the difference in RI is minimal.

(Fig. 3(a)) and gel (Fig. 3(b)) spectra, confirming the successful photopolymerization. In the IR spectra of the derivatives calcined at 800 °C (Fig. 3(d)), no peaks contributed to organic bonds are observed, indicating the complete decomposition of organic compounds and the formation of inorganics.

2.3 Thermogravimetric analysis

The thermal degradation and mass loss behavior (black curve), heat flow measurements (red curve), and rate of mass change (blue curve) are presented in Fig. 4. Decomposition from polymer to ceramic of YAG:0% Ce^{3+} (Fig. 4(a)) and YAG:2% Ce^{3+} (Fig. 4(b)) precursor samples synthesized via polymerization was investigated using thermogravimetric analysis (TGA) up to 900 °C under an oxygen atmosphere at a heating rate of 5 °C/min.

Mass changes result from evaporation, decomposition, combustion, and oxidation. The initial rapid weight loss (up to 6.3%/min) below 200 °C, accounting for 54.5%–56.6% of the total mass loss, is attributed to the evaporation of residual solvents (e.g. water, ethylene glycol) and low-molecular-weight species remaining after gelation. Above 250 °C, the thermal degradation of the polymeric samples proceeds in

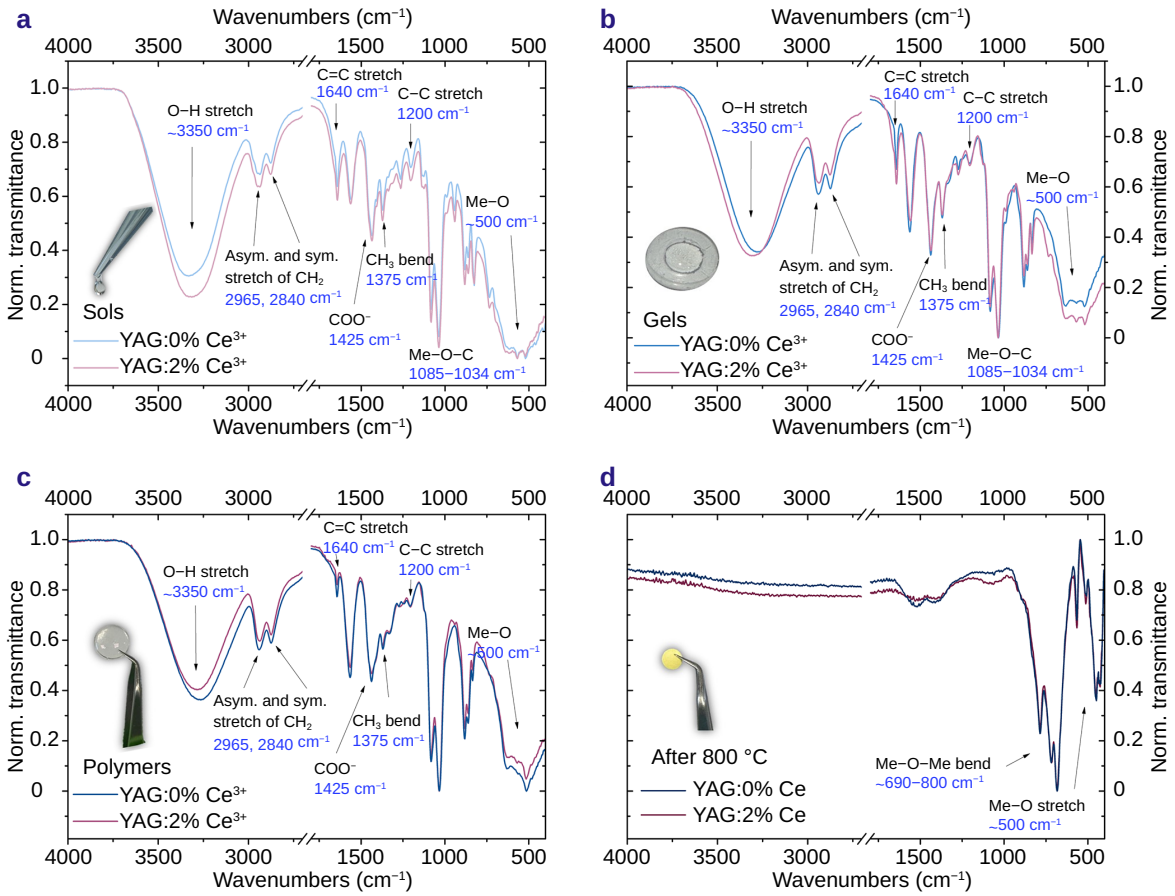

Fig. 3 | Fourier transform infrared spectroscopy (FT-IR) spectra of undoped YAG and YAG:2% Ce^{3+} sols (a), gels (b), polymers (c) and samples heated at 800 °C temperature in an air atmosphere (d) along with photographic images of the materials doped with 2% Ce^{3+} ions. Annealing the materials at temperatures of at least up to 800 °C effectively removes all organics.

three stages. In the first two stages (250 °C < t < 550 °C), endothermic processes lead to a mass loss of up to 18.5%, corresponding to the decomposition of organic components and polymerized network components originating from acrylic acid and propylene oxide-derived species, and the decomposition of metal-organic complexes (e.g. carboxylates and alkoxide-type bonds), as evidenced by FT-IR bands corresponding to C–H, C–O, COO^-, and Me–O–C groups. The third stage, occurring exothermally between 550 °C < t < 680 °C, is associated with combustion, resulting in a mass loss of 7.3% for YAG:0% Ce^{3+} and 7.4% for YAG:2% Ce^{3+}. At temperatures above 800 °C, further exothermic processes correspond to the oxidation of ceramic compounds. The residual mass at 900 °C is 17.2% for YAG:2% Ce^{3+} and 19.7% for YAG:0% Ce^{3+}.

Based on the TGA data and considering the substantial mass losses and rapid thermal processes, a slow heating rate of 0.5 °C/min up to 1000 °C was selected for the 3D objects to minimize structural deformations during solvent vaporization and precursor decomposition and to ensure uniform shrinkage and densification of the structure[47].

2.4 Quality and spatial resolution assessment of 3D microstructures

3D structures were fabricated to evaluate the suitability of the synthesized YAG:2% Ce^{3+} precursor for laser lithography. To determine the optimal processing parameters, 3D woodpile matrices (Fig. 5) were printed by varying the exposure power (50–250 mW corresponding to 0.7896–3.948 TW/cm^2 in 20 mW (0.3158 TW/cm^2) increments at the sample) and the scanning velocity (1–10 mm/s in 1 mm/s increments). The printed matrix is divided into zones, similar to that presented in ref.[48]: 3D objects outlined in blue correspond to suitable polymerization parameters, those in pink indicate partially suitable conditions, and those in red represent unsuitable conditions. Representative SEM images of individual structures from the matrix cells are shown below. It was observed that at low laser powers combined with the lowest scanning velocities, no structures were formed. At the maximum scanning velocity, the fabrication of structures also failed; under these conditions, the exposure dose was too low at medium laser powers, preventing the polymerization process from taking place. Based on SEM

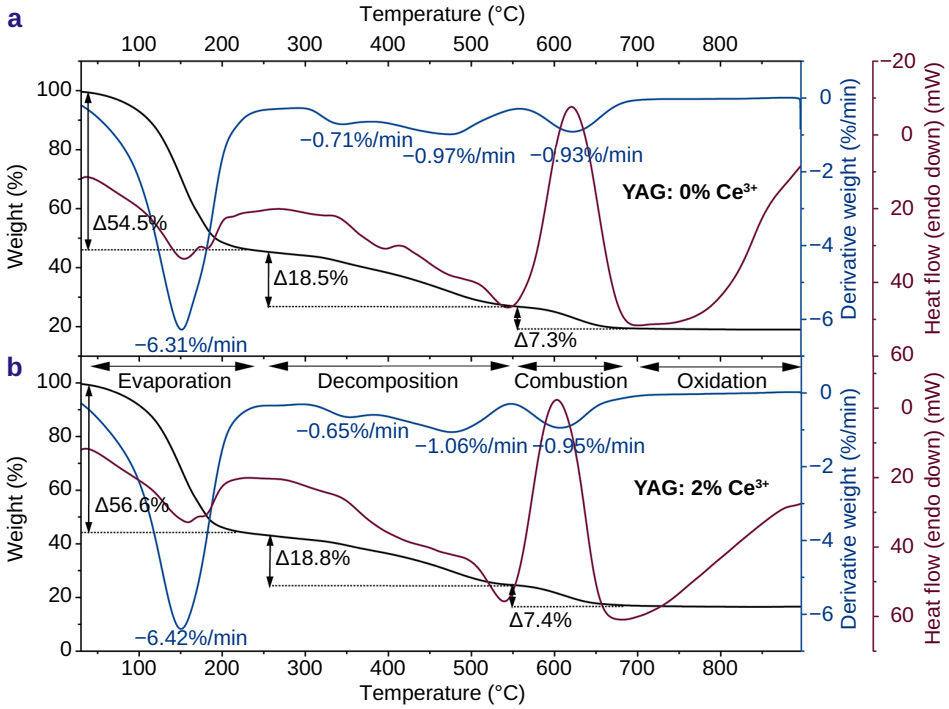

Fig. 4 | Thermogravimetric analysis data of synthesized (a) YAG:0% Ce^{3+}, (b) YAG:2% Ce^{3+} polymers: weight loss (black curve), derivative weight (blue curve), and heat flow (red curve) as a function of temperature.

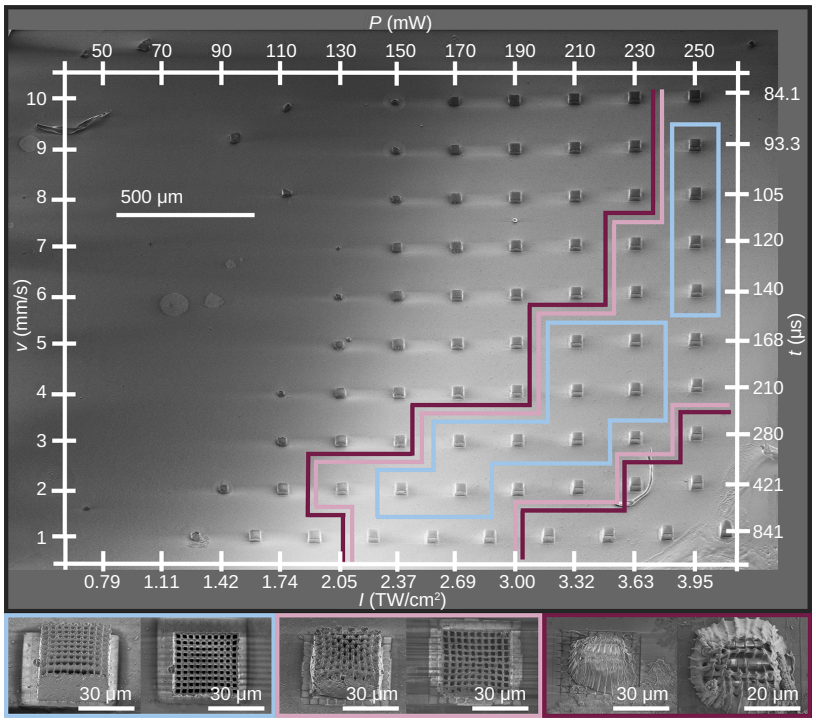

Fig. 5 | SEM images of an array of fabricated YAG:2% Ce^{3+} polymeric structures obtained by varying the laser power from 50–250 mW (0.7896–3.948 TW/cm^2) in 20 mW (0.3158 TW/cm^2) steps and the fabrication speed from 1 to 10 mm/s (exposure duration t = 84.1–841 μs) (in 1 mm/s steps). Higher-resolution SEM images of individual structures are shown below. The array is divided into zones: structures outlined in blue correspond to suitable polymerization parameters, in pink indicate partially suitable conditions, and in red represent unsuitable conditions.

image analysis, the most favorable fabrication conditions for small-scale structures were identified as follows: 150 mW (2.369 TW/cm^2) or 170 mW (2.685 TW/cm^2) at 2 mm/s, 170–210 mW (2.685–3.316 TW/cm^2) at 3 mm/s, 210 mW (3.316 TW/cm^2) or 230 mW (3.632 TW/cm^2) at 4 mm/s, 210 mW (3.316 TW/cm^2) or 230 mW (3.632 TW/cm^2) at 5 mm/s, and 250 mW (3.948 TW/cm^2) at 6–9 mm/s. These results demonstrate that the synthesized YAG:2% Ce^{3+} precursor exhibits well-defined processing windows suitable for laser multiphoton polymerization.

To evaluate the capabilities of the material, 3D structures with complex geometric shapes were manufactured by MP3DL and subsequently calcinated. Figure 6 presents SEM images of polymeric and crystalline 3D structures fabricated from the synthesized YAG:2% Ce^{3+} precursor. Two types of geometries were investigated: gyroid (Fig. 6(a, b)) and simple cubic lattice (Fig. 6(c, d)), as this configuration demonstrates the ability to produce truly cubic periodic 3D structures with slender features and is therefore most commonly used to study 3D fabrication capabilities. Polymeric structures (Fig. 6(a, c)) exhibit smooth surfaces and well-defined features, characteristic of multiphoton polymerization. After heat treatment at 1600 °C for 1 hour, the crystalline counterparts (Fig. 6(b, d)) show a significant reduction in overall dimensions due to shrinkage associated with polymer-to-ceramic conversion and by densification of the crystalline structure. Quantitative analysis reveals that the crystalline structures reach 60.7% and 61.5% of the linear dimensions of the initial polymeric objects in the directions marked as *x* and *y*, respectively. The difference is less than 1%, which could have been due to measurement deviations, confirming the isotropic shrinkage during the pyrolysis and crystallization process (see Fig. 6(c, d)). The highest resolution achieved was 2.40 μm (average 2.58 ± 0.17 μm) and the smallest feature size 0.48 μm (average 0.50 ± 0.03 μm) (see Fig. 6(b)) of crystalline gyroid, which is a significant

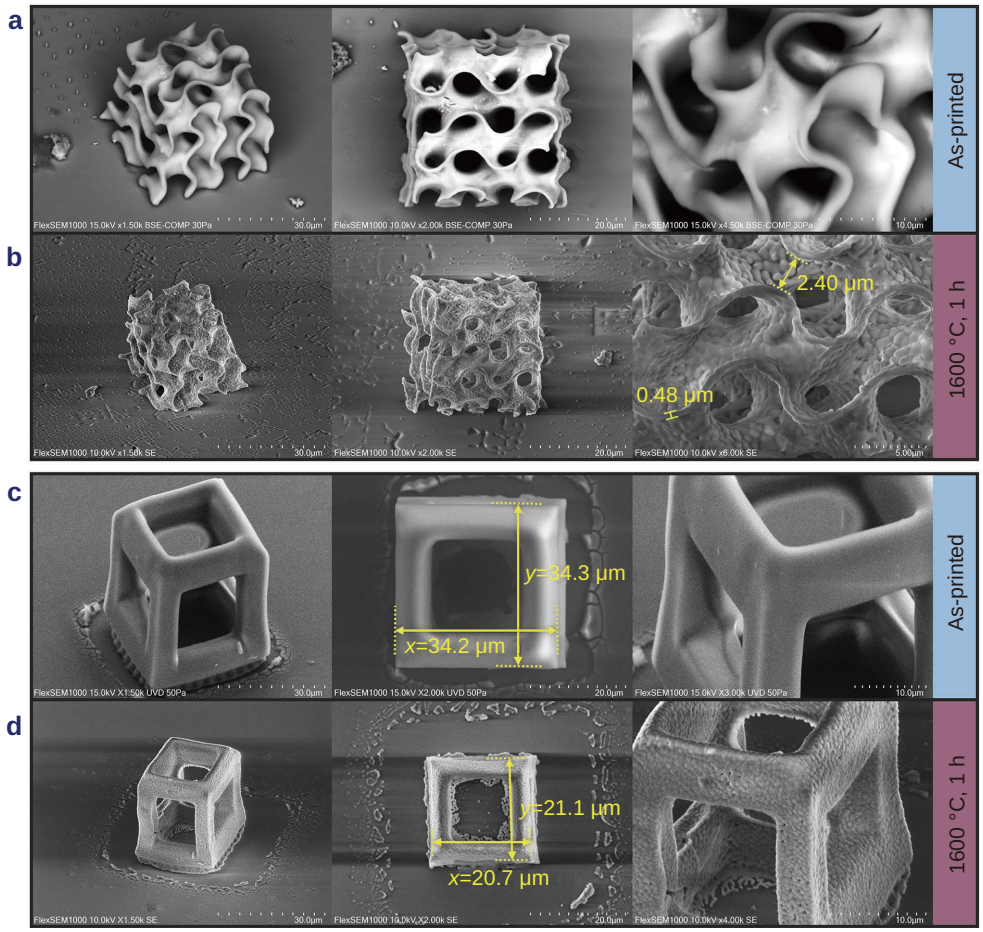

Fig. 6 | Scanning electron microscopy (SEM) images of polymeric (a, c) and crystalline (b; annealed at 1600 °C for 1 h) gyroid structures. The crystalline sample exhibits a minimum feature size of 0.48 μm (average 0.50 ± 0.03 μm) and a highest measured resolution of 2.40 μm (average 2.58 ± 0.17 μm). All individual measurements used to compute the averages are provided in Supplementary Fig. 1. (d) Cubic lattice, fabricated using YAG:2% Ce^{3+} precursor. The study of linear shrinkage after annealing at 1600 °C demonstrated that the dimensions of the crystalline structures were 60.7 (based on *x* value in images) and 61.5% (based on *y* value in images) of those of the original polymeric objects. Scale bars are indicated in each image.

improvement from the work by I. Cooperstein et al.[17], where the maximum achieved resolution was 3.8 μm and the smallest feature size was 2.3 μm①. All individual measurements used to compute the averages are provided in Supplementary Fig. S1.

Moreover, due to crystallites formation, the surface becomes rough, as can be seen in the Fig. 6(b) and 6(d). Surface roughness can reduce the efficiency of optical properties. The size distribution of the formed grains was investigated and discussed in the following section. Since the structural integrity and overall geometry were preserved, the synthesized precursor proved to be suitable for the fabrication of stable, high-resolution ceramic architectures.

2.5 Study of crystallization processes

The Fig. 7 presents a comprehensive structural and morphological analysis of YAG:Ce^{3+} 3D micro-objects subjected to high-temperature annealing. X-ray diffraction (XRD) analysis was performed to investigate the crystal structure and phase purity of the 3D-printed objects after thermal treatment. This direct 3D structural XRD measurement method was first demonstrated in 2022[3]. XRD patterns were recorded for YAG:0% Ce^{3+} powder as well as for YAG:0% Ce^{3+} and YAG:1% Ce^{3+} 3D micro-scaffolds. The samples were initially heated to 800 °C in air, followed by annealing in a reducing atmosphere consisting of 5% H_2 and 95% N_2 at 1600 °C for 1 hour. The reference pattern of $Y_3Al_5O_{12}$ from the Crystallography Open Database (COD 96-431-2143) is included in Fig. 7(a)). Debye-Scherrer rings generated during the XRD measurement (Fig. 7(b)) were integrated to produce the diffractogram of the YAG:1% Ce^{3+} 3D micro-object. The corresponding SEM image of the measured 3D micro-object is shown in Fig. 7(c).

XRD patterns (Fig. 7(a)) confirm the formation of a single phase cubic YAG structure in all samples examined, regardless of cerium doping concentration (0%, 1%) and sample form (powder or 3D printed micro-objects). The experimental XRD profiles closely match the reference pattern for $Y_3Al_5O_{12}$, indicating that Ce^{3+} incorporation does not significantly alter the crystal structure. Furthermore, a brief study was conducted to determine the maximum Ce^{3+} doping concentration that yields single-phase YAG under the present synthesis and annealing conditions. The diffractogram that presents these results is shown in Supplementary Fig. S2. Powder XRD analysis was employed to more sensitively detect the onset of secondary phase formation, as integration of Debye-Scherrer rings on the diffraction of 3D microstructures may not reveal minor impurity phases due to limited signal integration. Powder XRD patterns (Supplementary Fig. S2) indicate that compositions up to 5 mol-% Ce^{3+} remain single-phase YAG, while Rietveld refinement (Supplementary Table S1) shows an increase in the unit cell parameter *a*, indicating substitution at Y^{3+} sites. At 6 mol-% and above additional diffraction peaks attributable to impurities or secondary phases emerge, indicating that the maximum doping concentration of Ce^{3+} is 5 mol-%. The purity of a fabricated YAG:Ce^{3+} 5% woodpile structure was further assessed using scanning electron microscopy-energy-dispersive X-ray (SEM-EDX) with equipped focused ion beam (FIB) (Supplementary Fig. S3).

Debye-Scherrer rings (Fig. 7(b)) obtained from XRD measurements of a YAG:1% Ce^{3+} 3D micro-object annealed at 1600 °C for 1 h reveal a well-defined polycrystalline structure with uniform grain distribution and high crystallinity. However, in the diffractograms, weak peaks are observed between 10° and 12° 2Θ that do not match the reference data. These peaks can be disregarded as insignificant background artifacts arising during integration of the Debye-Scherrer ring image.

The morphological evolution of the 3D micro-objects due to annealing is illustrated in the SEM images (Fig. 7(c) and 7(d)). After 1 hour of annealing at 1600 °C, the 3D micro-objects retain well-defined structural features with relatively fine, small, porous and polyhedral grains (Fig. 7(c)). However, after 10 hours of annealing (Fig. 7(d)), significant grain coarsening occurs, leading to a more pronounced agglomeration. The grain geometry also changes to polyhedral and the porosity is reduced. This effect is quantitatively analyzed in the grain size distribution histograms (Fig. 7(e) and 7(f). The histogram for samples annealed for 1 hour (Fig. 7(e)) shows that the most common grain size falls within the range of 0.9 to 1.3 μm. In contrast, prolonged annealing for 10 hours (Fig. 7(f)) results in a shift toward larger grain sizes, with the most common range increasing from 1.5 to 3 μm. The grain size distributions are fitted with a normal-log model (black line), while the cumulative percentage curves further highlight the extent of grain growth over time —longer sintering leads to larger grains. Since shorter sintering times result in smaller grains, which should lead to lower light scattering and monophasic YAG/YAG:Ce—there was no need to prolong sintering any further.

Overall, these results demonstrate that the YAG phase remains stable across different doping concentrations and sample morphologies. However, high-temperature sintering has a significant impact on the microstructure, with prolonged annealing leading to substantial grain growth, exceeding a tenfold increase compared to shorter annealing durations. The shift in dominant grain size from 0.9–1.3 μm after 1 hour to 1.5–3 μm after 10 hours further emphasizes the pronounced grain coarsening effect. These findings provide valuable insights into the thermal behavior of YAG:Ce^{3+} 3D micro-objects, which is critical for optimizing

① Smallest feature sizes and resolution were not provided in the referenced article and instead were calculated by us from the SEM images.

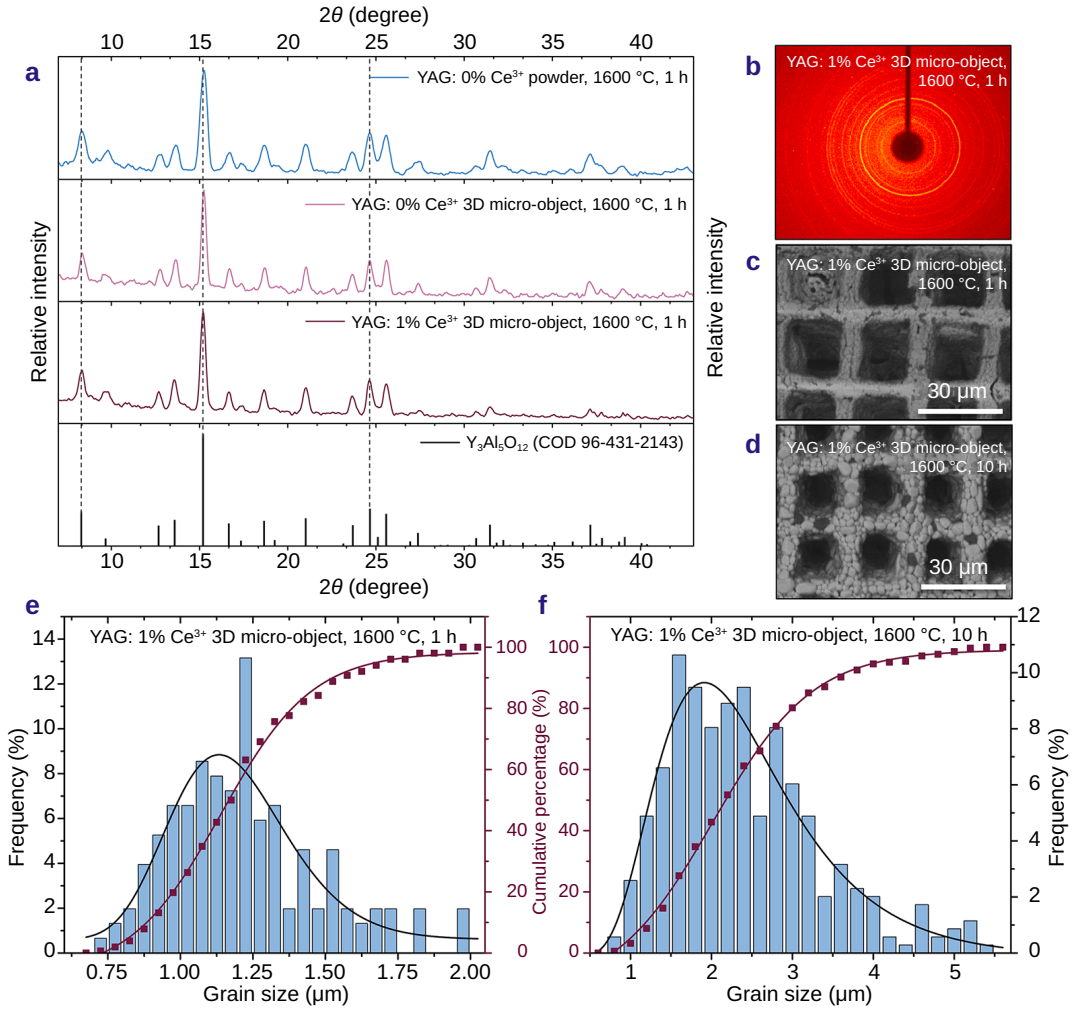

Fig. 7 | (a) X-Ray diffraction patterns of YAG: Ce^{3+} with mol-% concentrations of 0%, 1% 3D micro-objects annealed at 1600 °C for 1 hour, compared to synthesized YAG:0% Ce^{3+} powder annealed under the same conditions and the reference pattern of $Y_3Al_5O_{12}$ from Crystallography Open Database (COD). (b) Debye-Scherrer rings obtained from X-Ray diffraction measurement of a YAG:1% Ce^{3+} 3D micro-object annealed at 1600 °C for 1 hour. (c) Corresponding SEM image of a 3D micro-object. (d) SEM image of a YAG:1% Ce^{3+} 3D micro-object annealed at 1600 °C for 1 hour. (e, f) Histograms of grain size distributions along with the normal-log distribution curve (black) and cumulative percentage (carmine) corresponding to annealing durations of 1 hour and 10 hours, respectively. Regardless of dopant concentration or sample form (powder or 3D-printed object), the XRD patterns confirm a single-phase structure that matches the reference pattern of $Y_3Al_5O_{12}$ (COD 96-431-2143), verifying the formation of a pure cubic crystal structure. After 10 hours of annealing, the grain size increased more than tenfold compared to annealing for 1 hour.

their structural and functional properties.

2.6 Investigation of optical properties

Luminescence measurements were performed on 3D printed structures subjected to heat treatment at 1600 °C. A representative structure is shown in Fig. 8(c), while its optical image under 450 nm excitation is presented in Fig. 8(b). The sample exhibits visible emission with a characteristic yellowish-green color.

Emission spectra were recorded for YAG samples doped with 0.1%, 0.5%, 1%, 2% and 5% of Ce^{3+} (see Fig. 8(a)). The experimental setup employed for the luminescence characterization of the 3D microstructures is described in detail in the Luminescence characterization section. Under excitation at 450 nm, an emission band centered at 558 nm was detected, corresponding to the $[Xe]5d^1 \rightarrow [Xe]4f^1$ transition of Ce^{3+}. At 450 nm excitation the intensity of the emission was found to increase with increasing Ce^{3+} concentration, reaching its maximum at a doping level of 2%. Beyond this concentration, the intensity decreased, which can be attributed to the concentration quenching effect[49]. The weak additional emission features observed at ≈620 and ≈660 nm are not attributed to the intrinsic Ce^{3+} 5d–4f transition. These bands are likely associated with defect-related emission (oxygen vacancies) or trace impurity effects below

the SEM-EDX detection limit (≈0.1%). These results demonstrate that Ce^{3+} doped 3D-printed YAG structures exhibit efficient yellowish-green luminescence with optimal emission at 2% doping.

2.7 Comparison of current achievements

Figure 9 compares the reported feature sizes or spatial (lateral) resolutions of luminescent 3D structures fabricated via various lithographic techniques between 2009 and 2025[17–21,23,50,51,52–54]. Data points marked with an asterisk (*, next to the publication year on the *y*-axis) indicate cases where the reported dimensions were unavailable and thus approximated from published images. Over the past decade, significant progress has been made in reducing structural dimensions while maintaining optical functionality. However, most reported luminescent ceramics and hybrid materials still exhibit feature sizes exceeding several micrometers, which is much more than the employed emission wavelength. It is worth noting that the calcination procedure can, in principle, be localized using laser-thermal treatment if the substrate or surrounding media are sensitive to high temperatures[55].

In this context, our results, marked as a green star in the graph, demonstrate a major step forward. Our fabricated YAG:Ce^{3+} micro-architectures exhibit a minimum feature size of 0.50 ± 0.03 μm, representing, to the best of our knowledge, the smallest features achieved to date among luminescent crystalline materials produced by 3D lithography. Importantly, these structures are single-phase crystalline and intrinsically luminescent, combining optical functionality with sub-micron precision. Such a combination has not been previously demonstrated for single-phase YAG and highlights the potential of our approach based on sol-gel synthesis together with multiphoton fabrication and calcination routes for the development of Photonics Integrated Circuits (PICs)[56] and optoelectronic devices[57].

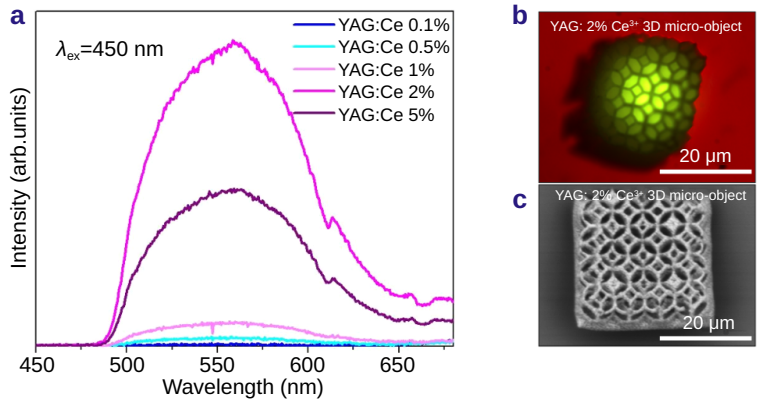

Fig. 8 | (a) Emission spectra of YAG:Ce^{3+} 3D micro-objects with Ce^{3+} concentrations of 0.1%, 0.5%, 1%, 2%, and 5% under 450 nm excitation. Additional emission at 690 nm attributed to chromium impurities from the furnace. (b) Photograph of YAG:2% Ce^{3+} 3D micro-object annealed at 1600 °C under 450 nm excitation. (c) SEM micrograph of YAG:2% Ce^{3+} 3D micro-object annealed at 1600 °C for 1 h.

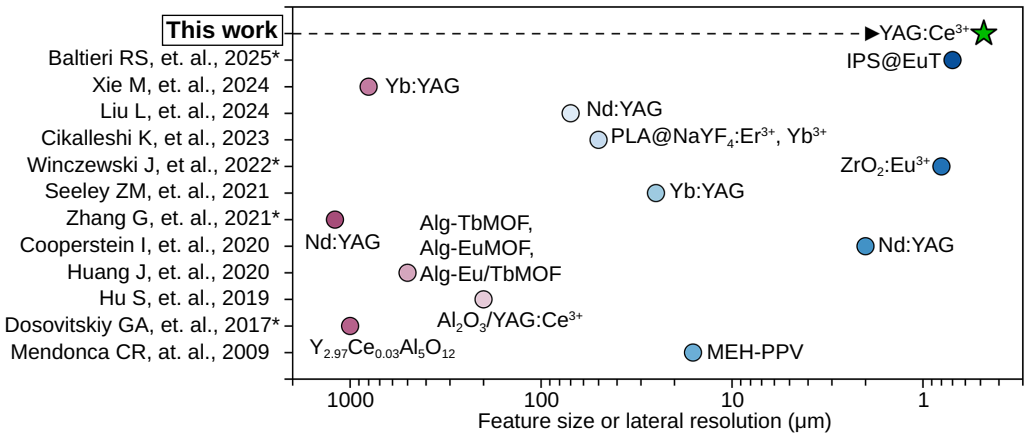

Fig. 9 | Current achievements in the feature size or resolution of luminescent 3D structures fabricated by 3D lithography from 2009 to 2025[17–21,23,50–51,51–54]. The values marked with an asterisk (*) next to the publication year on the *y*-axis correspond to those whose dimensions were not specified in the original article; therefore, they were approximately estimated based on the provided images. Our fabricated YAG:Ce^{3+} micro-architectures, marked as a green star, exhibit a minimum feature size of 0.50 ± 0.03 μm.

3 Conclusions

We established an end-to-end route engineering method for fabricating single-phase crystalline YAG:Ce^{3+} 3D micro-architectures with complex geometries and micrometer-scale features by combining precursor synthesis, MP3DL, and three-step annealing. Refractive indices measurements (436.5–643.3 nm) showed normal dispersion with minimal dependence on Ce^{3+} content (0–5 mol-%), and gel refractive indices ($n = 1.454–1.479$) matched coverslips and immersion oil, enabling deep, using high-NA laser direct writing. FT-IR/TGA verified polymerization and complete removal of organics by 800 °C, while a slow heating ramp of 0.5 °C·min^{-1} helped to preserve 3D geometry during conversion. Post-anneal at 1600 °C yielded single-phase crystalline YAG with isotropic linear shrinkage to 60.7%–61.5% of the polymer dimensions. The smallest feature size achieved was 0.50±0.03 μm (minimum 0.48 μm), and the highest measured resolution was 2.40 μm (average 2.58 ± 0.17 μm) of single-phase crystalline 3D micro structure. Under 450 nm excitation, Ce^{3+} emission peaked at 558 nm with maximum intensity of sample with 2 mol-% of Ce^{3+}. The results achieved enable the integration of YAG:Ce^{3+} microemitters and color conversion as high-temperature-resistant elements into optoelectronic and photonic devices-spanning LD/μLED-pumped light engines, on-chip waveguides and resonators, micro-scintillators, and biosensing microsystems, due to their resilience for use under extreme environmental conditions. This makes them excellent candidates for usage in open space applications under highly oscillating pressure and temperature.

4 Experimental

The experimental procedures employed in this study encompassed the synthesis of YAG:Ce^{3+} precursors, their structuring via MP3DL and subsequent thermal treatment, followed by comprehensive chemical, structural, and luminescence characterization of the fabricated 3D micro-objects.

4.1 Materials and synthesis

The following reagents were used in the study: hydrochloric acid (35%–38%, Chempur), yttrium oxide (99.99%, Tailorlux), ethylene glycol (analytical grade, Honeywell), aluminum chloride ($AlCl_3$) (98%, Merck), acrylic acid (99%, Sigma Aldrich), propylene oxide (99%, Alfa Aesar), cerium (III) acetate sesquihydrate ($Ce(CH_3COO)_3·1.5H_2O$) (an. gr., Alfa Aesar), diphenyl(2,4,6-trimethylbenzoyl)phosphine oxide (TPO)-a photoinitiator (97%, Sigma Aldrich), polydimethylsiloxane (PDMS) with a thermoinitiator (Sylgard 184), and Novec™ 7100 (≥99.5% Sigma Aldrich).

YAG:Ce^{3+} precursors were synthesized by the sol-gel method described in ref.[23]. For the calculation of doping level it is assumed that Y^{3+} was replaced by Ce^{3+} ions. The concentration of Ce^{3+} ions was set to 0, 0.05, 0.1, 0.2, 0.5, 0.7, 1, 2 and 5 mol-%. The representative synthesis of 1.000 g (1.685 mmol) YAG:2% Ce^{3+} is described below. Firstly, 0.5563 g (2.464 mmol) of yttrium oxide (Y_2O_3) was dissolved in 10 mL of hydrochloric acid in a 50 mL beaker. The solution was stirred using a magnetic stirrer and heated to 95 °C. 2 mL of distilled water was then added, and the solution was stirred further until it became clear. Once the yttrium oxide had dissolved, the solution was evaporated to obtain dry $YCl_3·xH_2O$. Next, 4.160 mL of an aqueous ethylene glycol solution containing 65% of ethylene glycol was added to the beaker with $YCl_3·xH_2O$ and stirred using a magnetic stirrer. After 5 minutes, 1.117 g (8.379 mmol) of aluminum chloride ($AlCl_3$) was added, and stirring continued. After another 5 minutes, 0.035 g (0.101 mmol) of $Ce(CH_3COO)_3·1.5H_2O$ was added, and the mixture was stirred for 30 minutes. Subsequently, 0.421 mL (6.014 mmol) of acrylic acid was added. After 30 minutes, 3.457 mL of propylene oxide was added in two portions (half immediately and the other half after 1 minute). The solution was then stirred for an additional 40 minutes. The resulting material was mixed with 1% TPO, and the solution was prepared for photopolymerization.

4.2 3D lithography and heat treatment

YAG:Ce^{3+} polymeric 3D objects were fabricated using a Laser Nanofactory femtosecond laser lithography workstation based on the MP3DL with control and automation software 3DPoli (Femtika Ltd.). The laser source was a Flint oscillator (Light Conversion), delivering 144 fs pulses at a repetition rate of 76 MHz, with a central wavelength of 1035 nm (517 nm second harmonic). Positioning stages ANT130-110-XY and ANT130-060-L-Z, together with AGV-10HPO galvanometric scanners (Aerotech), were employed. All experiments were carried out at 517 nm using a Mitutoyo M Plan Apo 50× objective (*NA* = 0.75) and a Zeiss 63× oil-immersion objective (*NA* = 1.4) with Immersol 518 F.

To optimize fabrication parameters, 3D woodpile arrays (similar to the one shown in Fig. 5) were printed while varying the laser power from 50 mW to 250 mW (0.7896–3.948 TW/cm^2) in 20 mW (0.3158 TW/cm^2) steps, and the scanning velocity from 1 mm/s to 10 mm/s in 1 mm/s increments. For the fabrication of larger-scale structures (hundreds of μm in size), the laser intensity was set to 1.105 TW/cm^2 and the scanning velocity to 10 mm/s. For smaller-scale structures (less than 100 μm), the laser intensity and scanning velocity were set to 0.1147 TW/cm^2 and 0.1 mm/s, respectively. Following fabrication, the polymerized YAG:Ce^{3+} precursor samples were immersed in ethanol to remove unpolymerized resin and subsequently rinsed with Novec 7100™ to completely eliminate residual solvent.

The thermal processing of the fabricated 3D micro-

objects was carried out in three stages. In the first stage, the objects were annealed at 800 °C for 1 hour in an air atmosphere, with a temperature ramp rate of 0.5 °C/min, to remove organic matter and carbon. This slow heating rate was selected based on thermogravimetric analysis, which indicated high rates of mass loss. The gradual heating ensured uniform shrinkage of the structures and minimized the risk of defects in the 3D objects. In the second stage, the objects were heated in an air atmosphere to 1600 °C at a rate of 10 °C/min and held for 1 hour. This process ensured the formation of a single-phase crystalline structure. In the final stage, the objects were treated in a mixture of 5% H_2 and 95% N_2 reducing atmosphere at 1000 °C for 1 hour, with a heating rate of 10 °C/min, reducing Ce^{4+} to Ce^{3+} and enhancing the luminescence properties of the 3D objects.

4.3 Chemical and structural characterization

Refractive indices of YAG precursor's sols, gels and polymers were collected using Abbemat WR MW equipped with a YAG (yttrium-aluminium-garnet) prism, LED source at wavelengths of 436.5, 486, 513.5, 546.3, 589.3, and 643.3 nm. Measurements were performed at 25 °C temperature.

FT-IR spectra of YAG precursor's sols, gels, polymers and discs heated at 800 °C in an air atmosphere, were recorded using FT-IR spectrometer ALPHA (Bruker, Inc.), equipped with a room temperature detector DLATGS. Spectra were acquired from 100 interferogram scans with 2 cm^{-1} resolution, from 4000 to 485 cm^{-1} wavenumbers.

For TGA analysis, Perkin Elmer Pyris 1 equipment was used; polymeric YAG discs were heated under an air atmosphere from 30 °C to 900 °C with a heating rate of 5 °C/min.

The SEM images of unsputtered 3D micro-objects before and after heat treatment were taken with a FE-SEM Hitachi SU-70. EDS of heated 3D micro-objects were taken with a lower resolution scanning electron microscope- Hitachi TM3000. The elemental analysis was carried out with 15 kV accelerating voltage.

The XRD data of 3D micro-objects and powder annealed at 1600 °C were directly collected on a BRUKER AXS (D8 Quest System) X-ray diffractometer equipped with PHOTON 100 cmOS detector. The X-ray generator was operated at 50 kV and 20 mA using Mo $K\alpha$ (λ = 0.71073 Å) (1 Å = 10^{-10} nm) radiation. Annealed 3D micro-structures and powders were placed on the measuring needle, obtained X-ray diffraction data Debye-Scherrer rings were collected and integrated using Bruker Apex 3 software. Obtained X-ray diffractograms were compared to the reference data from COD (Crystallography Open Database).

4.4 Luminescence characterization

The luminescence data on 3D micro-objects was obtained using a custom setup (Fig. 9) consisting of Light Conversion Pharos femtosecond Yb:KGW laser (λ = 1030 nm, τ_{pulse} = 300 fs) and Light Conversion Orpheus optical parametric amplifier (OPA) with Light Conversion Lyra second harmonic module as the illumination (excitation) source with the output wavelength set at 450 nm. The micro-objects were illuminated using Olympus plano-apochromat microscope objective lens (M = 10×, NA = 0.25). Luminescence emission was measured using Avantes AvaSpec ULS2048 UV-VIS-NIR spectrometer by directing the emission through the same objective lens and separating the emission from the illumination beam using Thorlabs longpass dichroic mirror (λ_{cutoff} = 490 nm). Accurate characterization of RI is intended future work as the current established methods are still not reliable for 3D free-form geometries at microscales[58].

References

1. Xu JL, Bu XH. Optical properties and applications of crystalline materials. *Adv Opt Mater* **9**, 2102394 (2021).
2. Xiao ZH, Yu SJ, Li YM et al. Materials development and potential applications of transparent ceramics: a review. *Mater Sci Eng R Rep* **139**, 100518 (2020).
3. Merkininkaitė G, Aleksandravičius E, Malinauskas M et al. Laser additive manufacturing of Si/ZrO_2 tunable crystalline phase 3D nanostructures. *Opto-Electron Adv* **5**, 210077 (2022).
4. Zhang XL, Ma KL, Wang S et al. Modulation of optical performances of YAG: Ce glass-ceramics for laser-driven lighting through doping with high thermal conductivity AlN. *Ceram Int* **51**, 52399–52408 (2025).
5. Liu JQ, Zhao XD, Xu YS et al. All-inorganic glass scintillators: scintillation mechanism, materials, and applications. *Laser Photon Rev* **17**, 2300006 (2023).
6. Drozdowski KJ, Witkowski ME, Makowski M et al. Luminescent and scintillation properties of GOS and GYAGG ceramics activated with cerium and praseodymium ions. *Ceram Int* **51**, 21182–21190 (2025).
7. Niterra. Ceramic type GOS scintillators. 2025-09-02. https://www.niterramaterials.co.jp/en/product/sc_cera.htm.
8. Feng SW, Guo YC, Allix M et al. Biphasic $Lu_3MgAl_3SiO_{12}$-based transparent ceramics for uniform laser-diode-driven white lighting. *Cell Rep Phys Sci* **3**, 101044 (2022).
9. Wu Z, Xu LM, Wang JD et al. Finely regulated luminescent Ag-In-Ga-S quantum dots with green-red dual emission toward white light-emitting diodes. *Opto-Electron Adv* **7**, 240050 (2024).
10. Harnik A, Merkininkaitė G, Ladika D et al. Laser 3D micro-/nano-structurization of luminescent materials. *Adv Opt Mater* **13**, 2500316 (2025).
11. Rosero-Arias C, Vásquez GC, Davila-Montero NG et al. Temperature promotes photoluminescence in lanthanide-doped 3D ceramic microarchitectures. *Adv Mater Interfaces* **11**, 2400339 (2024).
12. Chawla S, Roy T, Majumder K et al. Red enhanced YAG: Ce, Pr nanophosphor for white LEDs. *J Exp Nanosci* **9**, 776–784 (2014).
13. Lin SS, Lin H, Huang QM et al. Highly crystalline $Y_3Al_5O_{12}$: Ce^{3+} phosphor-in-glass film: a new composite color converter for next-generation high-brightness laser-driven lightings. *Laser Photon Rev* **16**, 2200523 (2022).
14. Li YG, Almeida RM. Preparation and optical properties of sol-gel derived thick YAG: Ce^{3+} phosphor film. *Opt Mater* **34**, 1148–1154 (2012).
15. Echartea-Reyes OA, Vázquez GV, Castillo-Robles JA et al. Syn-

thesis and characterization of Nd: YAG ceramics for laser applications. *Ceramics* **16**, 1655–1666 (2023).
16. Yao Q, Hu P, Sun P et al. YAG: Ce^{3+} transparent ceramic phosphors brighten the next-generation laser-driven lighting. *Adv Mater* **32**, 1907888 (2020).
17. Hu S, Liu YL, Zhang YL et al. 3D printed ceramic phosphor and the photoluminescence property under blue laser excitation. *J Eur Ceram Soc* **39**, 2731–2738 (2019).
18. Dosovitskiy GA, Karpyuk PV, Evdokimov PV et al. First 3D-printed complex inorganic polycrystalline scintillator. *CrystEngComm* **19**, 4260–4264 (2017).
19. Xie MM, Ji HH, Wang DW et al. 3D printing of gradient-doped Yb: YAG laser ceramics by leveraging active mixing. *Addit Manuf Front* **3**, 200118 (2024).
20. Seeley ZM, Phillips IR, Nerine TJR et al. Material jet printing of transparent ceramic Yb: YAG planar waveguides. *Opt Lett* **46**, 2433–2436 (2021).
21. Zhang GR, Wu YQ. Three-dimensional printing of transparent ceramics by lithography-based digital projection. *Addit Manuf* **47**, 102271 (2021).
22. Liu LY, Wang WB, Feng S et al. Rapid, micron-resolution 3D printing of Nd: YAG ceramic with optical gain. *Small* **20**, 2403130 (2024).
23. Cooperstein I, Indukuri SRKC, Bouketov A et al. 3D printing of micrometer-sized transparent ceramics with on-demand optical-gain properties. *Adv Mater* **32**, 2001675 (2020).
24. Skliutas E, Merkininkaitė G, Maruo S et al. Multiphoton 3D lithography. *Nat Rev Methods Primers* **5**, 15 (2025).
25. Bian P, Hu ZY, Liu XQ et al. Laser printing high-resolution inorganic 3D microstructures. *Laser Photon Rev* **20**, e01797 (2026).
26. Winczewski JP, Arriaga-Dávila J, Rosero-Arias C et al. Tailoring chemistry for inorganic 3D micro-optics. *Trends Chem* **6**, 58–61 (2024).
27. Wen XW, Zhang BY, Wang WP et al. 3D-printed silica with nanoscale resolution. *Nat Mater* **20**, 1506–1511 (2021).
28. Balčas G, Malinauskas M, Farsari M et al. Fabrication of glass-ceramic 3D micro-optics by combining laser lithography and calcination. *Adv Funct Mater* **33**, 2215230 (2023).
29. Bauer J, Crook C, Baldacchini T. A sinterless, low-temperature route to 3D print nanoscale optical-grade glass. *Science* **380**, 960–966 (2023).
30. Hong ZH, Ye PR, Loy DA et al. High-precision printing of complex glass imaging optics with precondensed liquid silica resin. *Adv Sci* **9**, 2105595 (2022).
31. Farsari M. Advances in 3D and 4D multi-photon printing for micro and nano photonics [Invited]. *Opt Mater Express* **15**, 2770–2791 (2025).
32. Hubert F, Bader T, Wahl L et al. Additive manufactured waveguide for E-band using ceramic materials. *Appl Sci* **12**, 212 (2022).
33. Volk A, Rai A, Agha I et al. Development of spatially variant photonic crystals to control light in the near-infrared spectrum. *Sci Rep* **12**, 16146 (2022).
34. Chepyga LM, Jovicic G, Vetter A et al. Photoluminescence properties of thermographic phosphors YAG: Dy and YAG: Dy, Er doped with boron and nitrogen. *Appl Phys B* **122**, 212 (2016).
35. Zhuo SF, Lin SS, Pang T et al. Transparent ceramic-quantum dots glass film composites with high-efficiency thermal management for laser-driven projection display. *Adv Funct Mater* **36**, e16371 (2026).
36. Kosyanov DY, Vornovskikh AA, Zavjalov AP et al. Influence of HIP post-treatment on the microstructure and luminescent properties of SPSed Al_2O_3-Ce: YAG composite ceramics. *J Alloys Compd* **1010**, 178153 (2025).
37. Li ZC, Wei YF, Zhao JZ et al. Innovative microstructure design of phosphor-in-glass film converter for efficient and high-brightness laser lighting. *Adv Opt Mater* **13**, e02398 (2025).
38. Liu X, Zhu YX, Cheng ZQ et al. Spectrum regulation of YAG: Ce/YAG: Cr/YAG: Pr phosphor ceramics with barcode structure prepared by tape casting. *J Am Ceram Soc* **107**, 1061–1069 (2024).
39. Yang ZZ, Lin SS, Zheng S et al. High-efficiency red-emitting phosphor-in-glass films for laser-driven lighting and display. *Laser Photon Rev* **20**, e02185 (2026).
40. Liao SX, Jin SL, Pang T et al. Novel color converters for high brightness laser-driven projection display: transparent ceramics-glass ceramics film composite. *Adv Funct Mater* **34**, 2307761 (2024).
41. Sang PF, Zhang L, Kang J et al. Composite structure Al_2O_3/Al_2O_3-YAG: Ce/YAG ceramics with high color spatial uniformity for white laser lighting. *J Adv Ceram* **13**, 189–197 (2024).
42. Ma XG, Li XY, Li JQ et al. Pressureless glass crystallization of transparent yttrium aluminum garnet-based nanoceramics. *Nat Commun* **9**, 1175 (2018).
43. Wang LH, Liu JW, Xu L et al. Realizing high-power laser lighting: artfully importing micrometer BN into Ce: GdYAG phosphor-in-glass film. *Laser Photon Rev* **17**, 2200585 (2023).
44. Zhang HJ, Zhao JZ, Yu ZK et al. A novel sapphire@PiGF@sapphire color converter with high luminescence saturation threshold for laser lighting. *Adv Funct Mater* **35**, 2414023 (2025).
45. Mettry M, Worthington MA, Au B et al. Refractive index matched polymeric and preceramic resins for height-scalable two-photon lithography. *RSC Adv* **11**, 22633–22639 (2021).
46. Douvdevany MYM, Paz D, Magdassi S. Fabrication of Ruby by 3D printing of transparent salt solutions. *J Eur Ceram Soc* **44**, 116773 (2024).
47. Gao YQ, Ding JJ. Low solid loading, low viscosity, high uniform shrinkage ceramic resin for stereolithography based additive manufacturing. *Procedia Manuf* **48**, 749–754 (2020).
48. Jonušauskas L, Gailevičius D, Mikoliūnaitė L et al. Optically clear and resilient free-form μ-optics 3D-printed via ultrafast laser lithography. *Materials* **10**, 12 (2017).
49. Merkininkaite G, Zabiliūtė-Karaliūnė A, Jüstel T et al. Ce^{3+} → Cr^{3+} energy transfer in $Y_3Al_3MgSiO_{12}$ garnet host and application in horticultural lighting. *Ceram Int* **49**, 16796–16808 (2023).
50. Baltieri RS, Reupert A, Manzani D et al. Remote luminescent temperature sensing using 3D-printed Eu(III)-doped micropolymers at the tip of an optical fiber. *Adv Mater Technol* **10**, 2401877 (2025).
51. Cikalleshi K, Nexha A, Kister T et al. A printed luminescent flier inspired by plant seeds for eco-friendly physical sensing. *Sci Adv* **9**, eadi8492 (2023).
52. Winczewski J, Herrera M, Cabriel C et al. Additive manufacturing of 3D luminescent ZrO_2: Eu^{3+} architectures. *Adv Opt Mater* **10**, 2102758 (2022).
53. Huang JH, Wu PY. Controlled assembly of luminescent lanthanide-organic frameworks via post-treatment of 3D-printed objects. *Nano-Micro Lett* **13**, 15 (2021).
54. Mendonca CR, Correa DS, Marlow F et al. Three-dimensional fabrication of optically active microstructures containing an electroluminescent polymer. *Appl Phys Lett* **95**, 113309 (2009).
55. Vangelatos Z, Wang L, Grigoropoulos CP. Laser pyrolysis for controlled morphing and chemical modification on 3D microlattices. *J Micromech Microeng* **30**, 055008 (2020).
56. Tian WC, Wang YF, Dang HJ et al. Photonic integrated circuits: research advances and challenges in interconnection and packaging technologies. *Photonics* **12**, 821 (2025).
57. Qi YF, Yue GC, Hao T et al. Strong-confinement low-index-rib-loaded waveguide structure for etchless thin-film integrated photonics. *Opto-Electron Adv* **8**, 250056 (2025).

58. Ryu M, Varapnickas S, Gailevicius D et al. Interferometric microscale measurement of refractive index at VIS and IR wavelengths. *SciPost Phys Core* **7**, 059 (2024).

Acknowledgements

This research has been carried out in the framework of the "Universities' Excellence Initiative" programme by the Ministry of Education, Science and Sports of the Republic of Lithuania under the agreement with the Research Council of Lithuania (project No. S-A-UEI-23-6) and was funded by Vilnius University Research Promotion Fund (project No. MSF-JM-10/2024).

Competing interests

Mangirdas Malinauskas serves as an Editor for the Journal, and no other author has reported any competing interests.

Supplementary information

Supplementary information for this paper is available at
https://doi.org/10.29026/oea.2026.250338